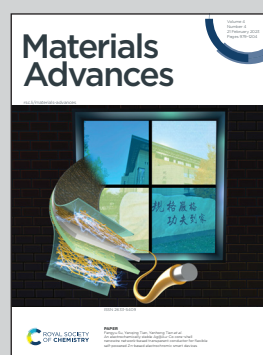


**Showcasing research from Professor Laurence Motte's Bionanomaterial group, Laboratory for Vascular Translational Science, University of Sorbonne Paris Nord, Île-de-France, France.**

Optical and X-ray attenuation properties of hafnium oxide nanoparticles surface functionalized with fucoidan: toward the early diagnosis of atherothrombotic diseases

Atherothrombosis is responsible for 30% of deaths due to a lack of early detection of the location of vascular diseases by conventional imaging systems. The diagnostic imaging system used in this pathology is mainly Computed Tomography (CT), based on differences in the X-ray attenuation of tissues. The primary limitations of CT are its relatively low soft-tissue contrast and sensitivity. Herein, we developed inorganic NPs made of hafnium oxide that were synthesized as nanocarriers and potential CT contrast agents to target arterial thrombi overexpressing P-selectin and detect the activated platelets.

**As featured in:**



See Laurence Motte *et al.*,  
*Mater. Adv.*, 2023, 4, 1011.

## PAPER

[View Article Online](#)  
[View Journal](#) | [View Issue](#)Cite this: *Mater. Adv.*, 2023,  
4, 1011

# Optical and X-ray attenuation properties of hafnium oxide nanoparticles surface functionalized with fucoidan: toward the early diagnosis of atherothrombotic diseases†

Yasmine Sebti, <sup>a</sup> Salim Si-Mohamed, <sup>bc</sup> Rachida Aid, <sup>ad</sup>  
Frederic Geinguenaud, <sup>a</sup> Mohand Chalal, <sup>e</sup> Yoann Lalatonne, <sup>af</sup>  
Frederic Chaubet, <sup>a</sup> Phalla Ou <sup>ag</sup> and Laurence Motte <sup>★a</sup>

Atherothrombosis is the main cause of death worldwide. An early diagnosis of this pathology is necessary to avoid serious clinical events. In this study, we report hafnium oxide nanoparticles (HfO<sub>2</sub> NPs) designed as a CT contrast agent for an emerging imaging technology named spectral photon counting computed tomography (SPCCT). SPCCT allows the specific detection and quantification of the contrast agent concentration, according to its K-edge. HfO<sub>2</sub> NPs were surface functionalized with fucoidan, a sulfated polysaccharide that has high affinity for P-selectin considered as a glycoprotein biomarker in atherothrombosis, and citrate ions as a control ligand. The physicochemical characterization of fucoidan coated HfO<sub>2</sub> NPs (HfO<sub>2</sub>@fucoidan NPs) was finely studied, and the influence of the coating agent on the UV absorption and photoluminescence properties was evidenced. The *in vitro* flow adhesion assay showed the specific binding of HfO<sub>2</sub>@fucoidan NPs to activated platelets under arterial flow. These NPs showed excellent biocompatibility on the HUVEC cell line and the enhancement of cell viability. Phantoms performed with SPCCT show that the value of the attenuation rate (A. R.) of HfO<sub>2</sub>@fucoidan NPs (27 HU ml mg<sup>-1</sup>) is greater (×1.7) than that of HfO<sub>2</sub>@citrate NPs (17 HU ml mg<sup>-1</sup>). A good correlation between the measured concentration and the references was obtained. These synthesized HfO<sub>2</sub>@fucoidan NPs appear as a new candidate for X-ray imaging for the molecular-scale diagnosis of atherothrombosis.

Received 10th November 2022,  
Accepted 14th January 2023

DOI: 10.1039/d2ma01026g

[rsc.li/materials-advances](https://rsc.li/materials-advances)

## Introduction

Atherothrombotic events represent the main cause of mortality and morbidity in the world,<sup>1,2</sup> involving both the arterial and the venous part of the circulation: myocardial infarction, ischemic stroke, aneurysms, peripheral arterial disease, atrial thrombus and embolisms, phlebothrombosis and pulmonary embolisms. Many thrombotic events could be diagnosed before dramatic complications occur. By using an adequate molecular targeting strategy (*e.g.*, molecules that bind specifically to thrombi), thrombotic sites could be diagnosed early, thereby representing a crucial indicator in the management of thrombosis through preventive therapies. However, the presence of thrombi does not immediately lead to the total obstruction of the blood vessels. Instead, non-occluding parietal thrombus often occurs.<sup>3</sup> However, not all pathological sites are at risk of catastrophic events. Adequately and efficiently diagnosed at an early stage, non-occluding thrombi could represent an appropriate indicator for thrombotic diseases. Hence, new diagnostics could be based on visualizing thrombus at the diseased

<sup>a</sup> Université Sorbonne Paris Nord and Université Paris Cité, INSERM, LVTS, F-75018 Paris, France. E-mail: [laurence.motte@univ-paris13.fr](mailto:laurence.motte@univ-paris13.fr)<sup>b</sup> Department of Cardiovascular and Thoracic Radiology, Louis Pradel Hospital, Hospices Civils de Lyon, 59 Boulevard Pinel, 69500 Bron, France<sup>c</sup> CREATIS, UMR 5220, Univ Lyon, INSA Lyon, University Claude Bernard Lyon 1, Lyon, France<sup>d</sup> Université de Paris, FRIM, UMS 034, INSERM, F-75018, Paris, France<sup>e</sup> Université Sorbonne Paris Nord, CNRS, CSPBAT, F-93017 Bobigny, France<sup>f</sup> Service de Biophysique et Médecine Nucléaire, Hôpital Avicenne AP-HP, F-93009 Bobigny, France<sup>g</sup> Département de Radiologie, Hôpital Bichat, Université de Paris, Assistance Publique Hôpitaux de Paris, Paris, France

† Electronic supplementary information (ESI) available: Representative TXRF spectrum of the HfO<sub>2</sub> NP sample and the corresponding calibration curves of HfO<sub>2</sub>@fucoidan NPs and HfO<sub>2</sub>@citrate NPs; FTIR spectra of HfO<sub>2</sub>@fucoidan NPs at the saturated ratio *R* = 14 before and after ultrafiltration; TGA curves; FTIR and Raman spectra of HfO<sub>2</sub> NPs, citrate and HfO<sub>2</sub>@citrate NPs; stability *versus* pH, in glucose 5%, NaCl 0.9%, DMEM and DMEM+ 10% FBS at various times, and the attenuation rate measured with a SPCCT system for the commercial gadolinium based molecular agent: DOTAREM<sup>®</sup>. See DOI: <https://doi.org/10.1039/d2ma01026g>



vascular wall rather than just assessing risk factors.<sup>4,5</sup> Detecting at an early stage the preliminary events of thrombosis would represent a significant advance in cardiovascular medicine. Platelet activation and aggregation is one of the main “molecular signatures” of thrombotic diseases, and represents a major link between inflammation, thrombosis and atherogenesis. P-selectin, expressed at the surface of platelets and endothelial cells upon activation, belongs to a family of glycoproteins whose carbohydrate moieties are known to play a critical role in the physio-pathological processes such as cell-cell interactions, cell growth, lymphocyte trafficking, thrombosis or inflammation.<sup>6,7</sup> By linking innate immunity with coagulation in the cardiovascular system, P-selectin represents an important molecular target for imaging and therapeutic approaches to intravascular clots *in vivo*.<sup>8,9</sup> Therefore, numerous efforts have been devoted to the development of contrast agents for the imaging of P-selectin.<sup>10–12</sup> These agents were either P-selectin antibodies or synthetic mimics of sialyl Lewis X (SLeX), the natural ligand of P-selectin.<sup>13,14</sup> Although effective, the cost of synthesis of these agents, including raw materials, and the use of antibodies limit the potential translation to clinical use. Several sulfated polysaccharides have also been described to bind to P-selectin. Among them, fucoidan is a polysulfated L-fucose mainly extracted from brown seaweed endowed with biological activities closely connected to its chemical composition, to the distribution of the sulfate groups along the polyfucose backbone and to its molecular weight.<sup>15</sup> Fucoidan is a naturally occurring mimic of SLeX<sup>16,17</sup> and exhibits *in vitro* nanomolar affinity for immobilized P-selectin as well as the lowest nonspecific binding.<sup>18</sup> 99mTc-radiolabeled fucoidan as well as fucoidan coated on ultrasmall superparamagnetic iron oxide nanoparticles (NPs) enabled the detection of vascular thrombi by scintigraphy and MRI, respectively, in rat models of thrombosis and heart ischemia.<sup>19,20</sup>

Hafnium oxide (HfO<sub>2</sub>) nanoparticles (NPs) are considered for a large variety of applications including optoelectronic, photocatalysis, scintillator, UV photosensor and biomedical applications.<sup>21–26</sup> In nanomedicine, HfO<sub>2</sub> NPs are mainly used as radiosensitizers in cancer radiotherapy<sup>27–30</sup> (NBTXR3, Nanobiotix, phase II–III clinical trial) as contrast agents for diagnostic X-ray imaging,<sup>26,31–33</sup> biosensors,<sup>26</sup> or radioluminescent scintillators.<sup>34</sup>

In this work, we will explore the potentiality of HfO<sub>2</sub> NPs as computed tomography (CT) contrast agents for the molecular imaging of atherothrombosis with K-edge imaging enabled by spectral photon counting CT (SPCCT) imaging. SPCCT is an emerging CT modality in the clinical field that can detect specifically and quantify accurately a large variety of atoms with high *Z* atomic numbers (including <sup>72</sup>Hf) by using the K-edge technique.<sup>35–43</sup> In addition, this modality allows a significant improvement of the spatial resolution in comparison to standard CT, for improving the depiction of small structures such as calcification, ulceration or thrombus encountered in different atherosclerotic processes.<sup>44–48</sup>

In a previous paper,<sup>49</sup> we optimized the synthesis of HfO<sub>2</sub> NPs through a sol-gel method associated with a microwave *via*

the benzyl alcohol route, with direct extraction and stabilization in water without any post-modification treatment. The monoclinic m-HfO<sub>2</sub> NPs, with an ellipsoidal shape (average major and minor axes of 8 and 4 nm, respectively), show strong absorption in the UV range and photoluminescence properties related to the presence of oxygen vacancies. Herein, the NP surface was functionalized using an electrostatic approach for the direct and one-step complexation with fucoidan (HfO<sub>2</sub>@fucoidan) or with citrate ions (control NPs, HfO<sub>2</sub>@citrate). The efficiency of the surface functionalization was carefully characterized using various physicochemical techniques (Raman and infrared spectroscopy, thermogravimetry analysis (TGA) and dynamic light scattering (DLS)). Interestingly, the UV-vis absorption spectrum of HfO<sub>2</sub>@fucoidan presents a high extinction coefficient in the UV range compared to the absorption spectrum of the non-functionalized and control NPs. In addition, exaltation (by a factor 8) of the photoluminescence (PL) emission spectrum was observed for the HfO<sub>2</sub>@fucoidan NPs. Such an effect was related to an increase of oxygen vacancy concentration after fucoidan surface functionalization. After incubation with human umbilical vein endothelial cells (HUVECs), transmission electron microscopy (TEM) images show better internalization of control NPs compared to HfO<sub>2</sub>@fucoidan NPs. Concomitantly 50% cell inhibition was observed after incubation with 42 mM citrate NPs whereas for fucoidan-NPs cell viability remains at 100%. The *in vitro* flow adhesion assay under arterial blood flow conditions shows the specificity of the interaction between activated platelets and HfO<sub>2</sub>@fucoidan NPs. SPCCT Phantom imaging indicated a higher value of the attenuation rate (A. R.) for HfO<sub>2</sub>@fucoidan NPs (factor 1.7) compared to HfO<sub>2</sub>@citrate NPs at 120 kVp. To our knowledge, no studies report the effect of surface functionalization of HfO<sub>2</sub> NPs on CT attenuation using an SPCCT system. Such an effect was correlated with different mass attenuation coefficients for HfO<sub>2</sub>@fucoidan NPs and HfO<sub>2</sub>@citrate NPs related to different mass fractions of citrate and fucoidan.

## Experimental

### Materials

The reagents for nanoparticle synthesis were hafnium(IV) chloride (HfCl<sub>4</sub>, 99.9%) from Alfa Aesar and benzyl alcohol (99%) from Acros Organics. The reagents were stocked in a glovebox (MB-Easylab V2.0 Braun) under a controlled atmosphere (O<sub>2</sub> < 0.5 ppm, H<sub>2</sub>O < 0.5 ppm). The NP water phase transfer was performed using dichloromethane (99%, Fisher Scientific). The pH was adjusted using hydrochloric acid (1 M) or sodium hydroxide (1 M) from Carlo Erba.

Low molecular weight fucoidan (batch #ASPHY12399) from the brown seaweed *Ascophyllum nodosum* was purchased from Algues & Mer (Ile d'Ouessant, France). Fucose and sulfate contents were 43 and 26, respectively (% w/w), with *M<sub>n</sub>* = 4100 g mol<sup>−1</sup> and *M<sub>w</sub>* = 10 800 g mol<sup>−1</sup>. Citric acid and rhodamine 123 were purchased from Sigma-Aldrich and Fisher Scientific, respectively. 1-Ethyl-3-(3-dimethylaminopropyl)carbodiimide (EDC), *N*-hydroxysuccinimide



(NHS), and *N* ethyl diisopropylamine were purchased from Fisher Scientific.

### HfO<sub>2</sub>-fucoidan-NP synthesis and surface functionalization

Non-coated NPs were synthesized by the reaction of hafnium(IV) chloride (140 mM with benzyl alcohol (10 ml) at 200 °C for 3 h under microwave irradiation, on a Monowave 300 from Anton Paar (Anton Paar GmbH, Graz, Austria) according to a procedure already described.<sup>49</sup> To coat the NPs with fucoidan, HfO<sub>2</sub> NPs dispersed in water at pH = 2 ([HfO<sub>2</sub>] ≈ 100 mM) were mixed with various amounts of fucoidan dissolved in water (pH = 7) under stirring for 2 hours, corresponding to a ratio *R* between 0 and 25, with *R* = 1000 ([fucoidan]/[HfO<sub>2</sub>]). The HfO<sub>2</sub>@fucoidan NPs were washed three times by ultracentrifugation (Amicon 100 kDa, Merck Millipore) and suspended in water. The pH was adjusted to 7.4 by the addition of NaOH (1 M).

The HfO<sub>2</sub> NPs were also surface functionalized with citrate ions and used as control NPs. HfO<sub>2</sub> NPs were dispersed in water at pH = 2 ([HfO<sub>2</sub>] ≈ 100 mM) and mixed for 2 hours under magnetic stirring with citric acid dissolved in water (pH = 3) with a mass ratio of 2 between the ligand and the NPs. After the reaction, the pH was adjusted to 7.4 by the addition of NaOH (1 M) and the NPs-citrate was washed three times by ultracentrifugation (Amicon 100 kDa, Merck Millipore) and suspended in water (pH = 7.4).

The NPs were also labelled with rhodamine 123. The carboxylate functions at the outer surface of HfO<sub>2</sub>@fucoidan and HfO<sub>2</sub>@citrate NPs ([Hf] = 50 mM) were activated using 1-ethyl-3-(3-dimethylaminopropyl)carbodiimide (EDC) and *N*-hydroxysuccinimide (NHS), [EDC] = [NHS] = 13 mM) at pH = 4, stirred for 2 h at 37 °C. The second step was the linkage of the amine function of Rhodamine-123 with the activated carboxylic acid functions on the NPs. The pH of the NP samples was adjusted to pH = 9 with *N* ethyl diisopropylamine. The Rhodamine-123 was dissolved in water at pH = 9 (adjusted with *N*-ethyl diisopropylamine) and then added to the samples and stirred for 24 h, under ambient temperature. The modified particles were washed 8 times by ultracentrifugation (Vivaspin 50 kDa) with deionized water. The NPs were redispersed in water at physiological pH.

### Physicochemical characterization

The Hf concentration was determined by the freeze drying process as described in a previous work<sup>49</sup> and by total reflection X-ray fluorescence spectrometry (TXRF, S2 PICOFOX, Bruker). For TXRF, calibration curves were first obtained using HfO<sub>2</sub>@fucoidan or HfO<sub>2</sub>@citrate solution (concentration of the stock solution determined after the freeze drying process), Fig. S1 (ESI<sup>†</sup>). TXRF data were collected over 300 s with a molybdenum tube excitation source operating at 50 kV/700 μA. Elemental concentrations were calculated using gallium standard solution (1 g L<sup>-1</sup>, Kraft GmbH) for each sample through the PICOFOX<sup>™</sup> software included in the equipment.

The hydrodynamic size and zeta potential of the NPs were investigated by dynamic laser light scattering (DLS) at a fixed

attenuator of 6 and a center position of 4.65 mm, using a Nano-ZS (Red Badge) ZEN 3600 device (Malvern Instruments, Malvern, UK). TEM images were obtained using an FEI Tecnai 12 (Philips), and the samples were prepared by depositing 10 μL of NP suspension on carbon-coated copper grids placed on a filter paper. The median diameter is deduced from TEM data measurements, simulating the diameter distribution with a log-normal function. The grafting of the fucoidan to the surface of the NPs was studied by Fourier transform infrared (FTIR) analysis, Raman analysis and thermogravimetric analysis (TGA). The FTIR spectra were recorded on a Bruker Tensor 27 FTIR spectrometer using the KBr pellet technique. The Raman measurements were performed on an Xplora spectrometer (Horiba Scientific-France) with a 660 nm excitation wavelength (diode laser). The sample as a solution was deposited on a microscopy glass and evaporated at 80 °C for 24 h. The spectra were recorded using a macro-objective with a magnification of 100× (NA = 1.2). To obtain a high resolution, a grating of 1800 T mm<sup>-1</sup> was used. The laser power used was 1 mW. Quantification of the number of fucoidan and citrate coated per NP was evaluated by TGA using a LABSYS Evo TG-DTA-DSC 16000 device from Setaram Instrumentation. The UV-visible and fluorescence properties of the NPs were studied using a V-630 UV-VIS Spectrophotometer (Jasco) and a Spex FluoroMax spectrofluorometer equipped with a Hamamatsu 928 photomultiplier (HORIBA Jobin Yvon, Villeneuve D'Ascq, France), respectively.

### Cell culture and cytotoxicity assay

The cytotoxicity of the HfO<sub>2</sub>@fucoidan and HfO<sub>2</sub>@citrate were evaluated on Human Umbilical Vein Endothelial cells (HUVECs) using the resazurin test. The cells were grown in DMEM supplemented with 10% (v/v) fetal bovine serum, 4 mmol L-glutamine, 100 U ml<sup>-1</sup> penicillin, and 100 μg ml<sup>-1</sup> streptomycin and kept in an incubator at 37 °C in a humidified atmosphere of 5%. The cells were seeded at 10 000 cells per well in a 96-well plate. After 24 h of incubation, the cell culture medium was removed and replaced by 200 μl of NP solution (in NaCl 0.9%) at various concentrations ranging from 0 (positive control) to 42 mM. The cells were incubated for another 24 h. To measure the cell metabolic activity, the medium was removed and replaced with 100 μL of Resazurin solution (10%), and the plates were covered in foil and incubated for 2 h. The fluorescence signal of Resazurin was monitored using 540 nm excitation and 590 nm emission wavelengths on an Infinite<sup>®</sup> 200 PRO microplate reader (TECAN Group Ltd, Männedorf, Switzerland). The obtained fluorescence (FI) values were blank corrected, and the relative cell viability was expressed as (FI<sub>NPs</sub>/FI<sub>control</sub>) × 100%, where FI<sub>control</sub> was obtained in the absence of the NPs. The experiment was performed in hexaplicate.

### Transmission electron microscopy (TEM) of NP-loaded HUVEC cells

For TEM imaging, 2 × 10<sup>6</sup> HUVEC cells were cultured in a 6-well plate. After 24 h of incubation, the cell culture medium is removed and replaced with 1 ml of HfO<sub>2</sub>@fucoidane or HfO<sub>2</sub>@citrate (2 mM, 12 mM and 32 mM) for another 24 h of incubation.



The cells were then washed with PBS and fixed for 1 h with 2% paraformaldehyde (PFA), and 1% glutaraldehyde diluted in PBS 1× and water. After 3 washes with PBS, the cells were maintained at 4 °C. For the observation with TEM, the samples were included in Epon and ultra-sectioned. The sections were deposited onto copper grids for observation with a TECNAI 12 electron microscope.

### Flow microchamber experiments

An *in vitro* flow adhesion assay was performed to assess the binding affinity of HfO<sub>2</sub>@fucoidan for P-selectin expressed on activated blood platelets<sup>50,51</sup>. Micro-channels of Vena8 Fluoro + chambers (width: 0.04 cm, height: 0.01 cm, and length: 2.8 cm; Cellix Ltd, Dublin, Ireland) were coated overnight with 100 µg ml<sup>-1</sup> collagen and then rinsed with NaCl 0.9%. Human whole blood was perfused under an arterial flow for 5 min (shear stress 67.5 dyne cm<sup>-2</sup>) leading to the formation of aggregated and activated blood platelets deposited on the micro-channels covered by collagen. The Rh123 labelled HfO<sub>2</sub>@fucoidan and HfO<sub>2</sub>@citrate (negative control) were injected under an arterial flow for 5 min. The binding and accumulation of the NPs were observed in real time by fluorescence microscopy (Axio Observer, Carl Zeiss Microscopy, Oberkochen, Germany). Fluorescence images were taken along each micro-channel after washing with NaCl 0.9%.

### Statistical analysis

The results are expressed as the mean ± SEM of at least three independent experiments. Statistical analysis was performed using an ANOVA test. Differences were considered significant when  $P < 0.05$ .

### NP phantom preparation for spectral photon-counting computed tomography (SPCCT)

The SPCCT system (Philips research and development; Haifa, ISRAEL) is a large field-of-view (50 cm in-plane) clinical prototype CT equipped with energy-sensitive photon-counting detectors (PCDs). Pixel pitch is of 275 × 275 µm<sup>2</sup> at the isocenter, bonded to Philips' proprietary ChromAIX2 application-specific integrated circuit, relying on the direct conversion high band gap semiconductor of cadmium zinc telluride. Z-coverage is 17.6 mm and the minimal rotation time of the gantry is 0.33 s. Each channel offers pulse-height discrimination with five controllable energy thresholds set as 30, 51, 64, 72 and 85 keV in order to allow the energy-based discrimination of Hafnium.<sup>52</sup> Further technical details are provided in previous studies.<sup>38,53</sup> A custom-made polyoxymethylene cylindrical phantom with a diameter of 10 cm and 12 holes with 1 cm diameter was used. The samples were loaded into the phantom using 1.5 ml polypropylene centrifuge tubes. Two sets of 12 tubes were prepared, each containing HfO<sub>2</sub>@fucoidan or HfO<sub>2</sub>@citrate NPs diluted in glucose (5%) with various concentrations. The concentrations (mg ml<sup>-1</sup>) of the NPs depended on the corresponding attenuation at 120 kVp. The target attenuation for each solution was chosen within the clinical standard for CT angiography applications, *i.e.* 280 Hounsfield units (HU) approximately. Hence, the NP concentration was in the range of 0–15 mg ml<sup>-1</sup>.

Five axial scans were performed using a conventional X-ray tube with a voltage of 120 kVp and a current of 100 mA. Conventional images scaled in Hounsfield units and spectral images scaled in mg ml<sup>-1</sup> of materials were reconstructed using 1 mm slice thickness, a field-of-view of 220 mm in-plane and a matrix of 512 mm. Spectral images consisted of reconstructing three materials, *i.e.*, 2 non-K-edge materials (water and iodine) and a K-edge Hafnium image. It is noted that a water image approximates the water content in the tissue even in the presence of contrast agents.

## Results and discussion

### HfO<sub>2</sub>@fucoidan NP synthesis and physicochemical characterization

Ellipsoidal HfO<sub>2</sub>-NPs with average major (2a) and minor (2b) axes of 8 and 4 nm (Fig. 1A) were synthesized using microwave non-aqueous sol-gel synthesis in a two-step process, following a procedure described previously.<sup>49</sup> NPs were surface functionalized with fucoidan, a negatively charged polysaccharide, or with citrate, one of the most used coating agents, using an electrostatic approach for the direct and one-step complexation<sup>54</sup> and taking care of the avidity effect of carboxylate (fucoidan, citrate) and sulfate (fucoidan) groups for the oxide surface.<sup>55</sup> To our knowledge, we reported herein a simple process for the direct and one step complexation of the HfO<sub>2</sub> NP surface. As shown recently,<sup>56</sup> water soluble HfO<sub>2</sub> NPs were obtained after ligand exchange from apolar NPs (dispersed in toluene) using at least 3 precipitation-redispersion cycles (starting from dispersion in toluene, and then re-dispersion in ethanol, and later on in methanol and finally in water). To saturate the HfO<sub>2</sub> NP surface with fucoidan, increasing amounts of polymer ( $R = 1000 \times [\text{fucoidan}]/[\text{Hf}]$ ) were added to HfO<sub>2</sub> NPs dispersed in acidic water (pH = 2, [Hf] = 100 mM). Under these conditions, hydroxyl ions onto the HfO<sub>2</sub> surface led to a positive surface charge, increasing the electrostatic interaction and chelating bridging with the polymer after mixing. After surface functionalization, the NPs

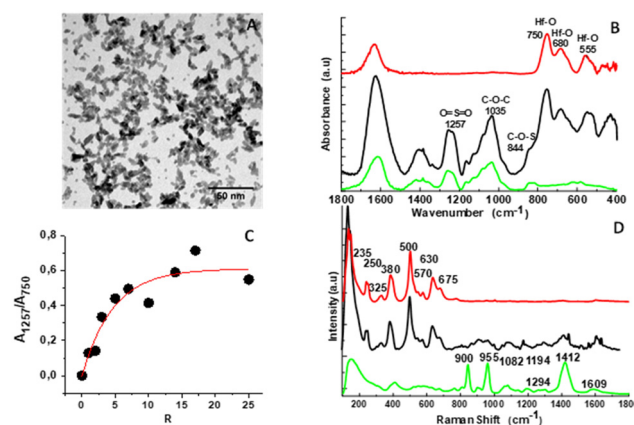


Fig. 1 Physicochemical characterization of HfO<sub>2</sub>@fucoidan NPs: TEM image (A), FTIR spectra (B) and evolution of the FTIR surface bands  $A_{1257}/A_{750}$  versus  $R$  (C), and Raman spectra (D) of HfO<sub>2</sub> NPs (red curve), fucoidan (green curve) and HfO<sub>2</sub>@fucoidan NPs (black curve).





were filtered to remove the unreacted chemical species. Surface coating was evidenced by FT-IR spectra, (Fig. 1B). In the 1500–500  $\text{cm}^{-1}$  region, the IR spectrum of fucoidan<sup>57</sup> was characterized by three peaks observed at around 1257  $\text{cm}^{-1}$  (O=S=O stretching), 1035  $\text{cm}^{-1}$  (C–O–C stretching) and 844  $\text{cm}^{-1}$  (C–O–S bending). The IR spectrum of the NPs present bands at 530, 555, 650, 680, and 750  $\text{cm}^{-1}$  in good agreement with IR phonon modes predicted for the monoclinic  $\text{HfO}_2$  phase.<sup>58</sup> After complexation with the NP surface, the IR fucoidan bands were also displayed on the spectra of  $\text{HfO}_2$ @fucoidan NPs in addition to the Hf–O characteristic vibration bands. Fig. 1C shows the evolution of the IR surface band ratio  $A_{1257}/A_{750}$  versus  $R$ . The signal rose with the increase of the molar ratio up to  $R \sim 14$ , to reach a plateau. This indicated an increase in the number of fucoidan molecules on the surface of the  $\text{HfO}_2$  NPs with an  $R$  ratio and saturation at  $R = 14$ . Considering the surface band ratio  $A_{1257}/A_{750}$  at this saturated ratio, before and after ultrafiltration, the average number of fucoidan molecules per NP was estimated to be  $\sim 70$  fucoidan per NP (Fig. S2, ESI†).

The coating was also evidenced by Raman spectroscopy and thermogravimetric analysis (TGA). Comparison of the Raman spectra of coated NPs with those of the native polysaccharide<sup>57</sup> and bare  $\text{HfO}_2$  NPs evidenced the organic layer around the NP, Fig. 1D. The TGA thermogram (Fig. S3, ESI†) exhibits a two-step decomposition: (i) the removal of water up to 200 °C that was estimated to be 3.25% (w/w) and (ii) the consecutive full degradation of the organic layer at around 900 °C. The overall weight loss (9.75% (w/w) for  $\text{HfO}_2$ @fucoidan NPs allowed the estimation of an average quantity of molecules per NP approximated to 65 in good accordance with the IR result.

The Raman and FTIR spectra of control NPs ( $\text{HfO}_2$ @citrate NPs) show the characteristic citrate and Hf–O bands, indicating an effective citrate surface complexation (Fig. S4, ESI†). The TGA thermogram (Fig. S5, ESI†) indicates an average of 800 citrate per NP. Considering an average number of 1440 hafnium onto the NP surface, this indicates that, as observed with iron oxide NPs,<sup>59</sup> two carboxylate functions per molecule are involved in two hafnium surface complexation and that the surface is fully saturated by citrate ions.

After coating, the NPs exhibit a hydrodynamic diameter at physiological pH (in intensity) of 58 nm (PDI = 0.2) and 33 nm (PDI = 0.4), and a negative charge surface of  $-27$  mV and  $-33$  mV for  $\text{HfO}_2$ @fucoidan NPs and  $\text{HfO}_2$ @citrate-NPs, respectively (Fig. S6, ESI† for pH stability). The NPs were also dispersed in glucose (5%) or in NaCl (0.9%), Fig. S7 (ESI†). A slight increase of the hydrodynamic diameter in the two media and after 1 day was observed for  $\text{HfO}_2$ @fucoidan NPs whereas the size does not change for  $\text{HfO}_2$ @citrate-NPs (Fig. S7, ESI†). In addition, better stability with time (measurement of the hydrodynamic diameter after 10 days) is observed for both NPs in glucose compared to NaCl medium (Fig. S7, ESI†).

### Influence of surface functionalization on the optical properties

Fig. 2 presents the UV-vis absorption and photoluminescence (PL<sub>em</sub>) spectra of the  $\text{HfO}_2$  (pH = 2,  $[\text{HfO}_2] = 1$  mM),  $\text{HfO}_2$ @citrate and  $\text{HfO}_2$ @fucoidan NPs (PH = 7.4,  $[\text{HfO}_2] = 1$  mM).

The UV-visible spectra of  $\text{HfO}_2$  and  $\text{HfO}_2$ @citrate were similar whereas the  $\text{HfO}_2$ @fucoidan sample presents a high extinction coefficient in the UV range, Fig. 2A. Considering an average of  $\sim 70$  fucoidan per NP, a concentration of  $\text{HfO}_2$  equal to 1 mM corresponds to about 6  $\mu\text{M}$  fucoidan. Fig. 2A inset shows the absorption spectrum of fucoidan at a concentration of 6  $\mu\text{M}$ . Clearly, the higher molar attenuation coefficient is not related to the UV absorption of fucoidan. This increase of UV absorption was observed in the case of  $\text{HfO}_2$  films with reduced oxygen content and was attributed to the higher concentration of oxygen vacancies.<sup>60,61</sup>

Polysaccharides are used as a reducing agent as well as a surface stabilizing template for the NPs.<sup>62</sup> One explanation<sup>63</sup> could be that more  $\text{Hf}^{3+}$  species are formed by the reduction function of fucoidan compared to sodium citrate. This higher ratio of  $\text{Hf}^{3+}/\text{Hf}^{4+}$  for  $\text{HfO}_2$ @fucoidan compared to  $\text{HfO}_2$ @citrate results in the creation of more surface oxygen vacancies to maintain charge balance.

After excitation at 200 nm wavelength, the PL<sub>em</sub> spectra of  $\text{HfO}_2$  and  $\text{HfO}_2$ @citrate were similar and present two emission bands centered at 325 (3.8 eV, blue transition) and 522 nm (2.4 eV, middle red transition) Fig. 2B and C. This PL<sub>em</sub> profile was attributed, in a previous paper,<sup>49</sup> to the oxygen vacancies inducing defect levels located deep in the band gap. The PL<sub>em</sub> spectra for nude NPs were deconvoluted with 4 Gaussian fits centered at 305 nm (4.1 eV, band I), 381 nm (3.2 eV, band II), 522 nm (2.4 eV, band III), and 675 nm (1.8 eV, band IV).

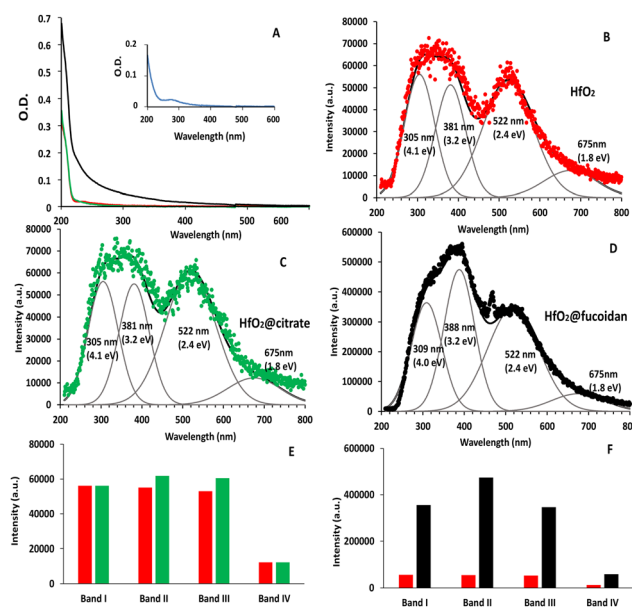


Fig. 2 (A) UV-Visible absorption spectrum of  $\text{HfO}_2$  (red curve [ $\text{HfO}_2$ ] = 1 mM, pH = 2),  $\text{HfO}_2$ @fucoidan (black curve) and  $\text{HfO}_2$ @citrate (green curve) NPs ( $[\text{HfO}_2]$  = 1 mM, pH = 7). Inset: UV-Visible absorption spectra of fucoidan in water ( $[\text{fucoidan}]$  = 6  $\mu\text{M}$ , pH = 7). (B–D) PL emission and deconvolution of the PL<sub>em</sub> spectrum using a Gaussian fit (grey curve) for  $\text{HfO}_2$  (red curve, B),  $\text{HfO}_2$ @citrate (green curve, C) and  $\text{HfO}_2$ @fucoidan (black curve, D) NPs ( $[\text{Hf}]$  = 1 mM,  $\lambda_{\text{ex}}$  = 200 nm). (E and F) comparison of the evolution of the PL intensity bands between (E)  $\text{HfO}_2$  (red bars) and  $\text{HfO}_2$ @citrate (green bars) NPs and (F)  $\text{HfO}_2$  (red bars) and  $\text{HfO}_2$ @fucoidan (black NPs).



522 nm (2.4 eV, band III) and 675 nm (1.8 eV, band IV). The emission peaks at 381 nm and 522 nm were assigned to  $\text{VO}_3$  with recombination to the valence band and to the defect level, respectively, and the band at 675 nm to the presence of interstitial oxygen defects. The PL component centered at 305 nm was either assigned to the vibronic transition of the excited  $\text{OH}^{\bullet*}$  radical (hydroxyl ions at the surface of the NPs) or to the self-trapped exciton.<sup>64–66</sup> Considering that the latter band was already observed after fucoidan or citrate surface functionalization, this favors the hypothesis of the self-trapped exciton. For  $\text{HfO}_2$  the intensity of the bands at 305 nm, 381 nm and 522 nm were quite similar and the contribution of the 675 nm band is lower ( $\approx 80\%$  lower compared to bands I and III) (Fig. 2B and E). After surface functionalization with citrate, a slight increase of the intensity of bands II and III was observed whereas the intensity of the other bands (I and IV) does not change compared to  $\text{HfO}_2$  (Fig. 2E). An exaltation of the emission (by a factor 8) was observed for  $\text{HfO}_2$ @fucoidan NPs (Fig. 2F) and the contribution of the band II increased. The best deconvolution of the  $\text{PL}_{\text{em}}$  spectrum was obtained with 4 Gaussian fits centered at 309 nm (4.0 eV, band I), 388 nm (3.2 eV, band II), 522 nm (2.4 eV, band III) and 675 nm (1.8 eV, band IV), Fig. 2D. Hence the positions of bands I and II are slightly red shifted compared to those of  $\text{HfO}_2$  and  $\text{HfO}_2$ @citrate NPs. In addition, the intensity of bands I and III remains quite similar whereas band II increases by a factor of  $\approx 31\%$ . Finally, the contribution of band IV remains  $\approx 80\%$  lower compared to bands I and III as observed for  $\text{HfO}_2$  and  $\text{HfO}_2$ @citrate NPs.

The proportions of each defect were estimated thanks to the area of each Gaussian function,<sup>67</sup> Table 1. Briefly, the amount of self-trapped exciton (band I) and interstitial oxygen defects (band IV) is found to be constant in the three samples with mean percentages of 25% and 9%, respectively. The proportion of band II ( $\text{VO}_3$  with recombination to the valence band) is quite similar (24%) for nude and citrate coated NPs and increases for  $\text{HfO}_2$ @fucoidan NPs (31%). Finally, the proportion of band III ( $\text{VO}_3$  with recombination to the defect level) is again quite similar (42%) for nude and citrate coated NPs and slightly decreases for  $\text{HfO}_2$ @fucoidan NPs (38%). These results suggest that band II is related to surface oxygen vacancies.

The efficiency of a PL emission is contributed to both by radiative and non-radiative recombination processes. Radiative recombination, related to oxygen vacancy concentration, increases the PL intensity while non-radiative recombination induces the opposite effect. The non-radiative transition is

initiated by defects present on the surface.<sup>67</sup> It is well known that the passivation of some surface defects by the capping ligands could affect wavelength shifts and variations of the intensities of the emission bands.<sup>68,69</sup> Surface defects act as the centers of non-radiative recombination for electrons and holes and promoting their passivation can raise the probability of radiative transitions.

Comparing  $\text{HfO}_2$ @citrate and  $\text{HfO}_2$ @fucoidan *versus*  $\text{HfO}_2$  NPs, the large difference in emission intensity in favor of the  $\text{HfO}_2$ @fucoidan NPs could be explained by an increase of surface oxygen vacancy concentration. This effect could be due to the more effective reductive effect of fucoidan compared to citrate and to a better complexation of the surface of the NP with the sulfate groups of fucoidan with respect to the carboxylate groups of citrate.<sup>70</sup>

### Influence of surface functionalization on HUVEC cell internalization and cytotoxicity

We first studied the  $\text{HfO}_2$ @fucoidan and  $\text{HfO}_2$ @citrate NPs (dispersed in NaCl 0.9%) internalization on stimulated fetal bovine serum-(SVF) human umbilical vein endothelial cells (HUVECs) using TEM. The cells were incubated for 24 h with three extracellular Hf concentrations: 2 mM, 12 mM and 32 mM. TEM imaging of the cells containing both types of NPs, one day after their internalization is shown in Fig. 3. They evidence (i) the endosomal confinement of the NP, with no differences in the intracellular location observed depending on the coating, (ii) the NP cell internalization increases upon increasing the incubation concentration as observed by us and others, (iii) better internalization of  $\text{HfO}_2$ @citrate NPs compared to  $\text{HfO}_2$ @fucoidan NPs. This latter effect can be related to high aggregation of  $\text{HfO}_2$ @citrate dispersed in NaCl 0.9% and DMEM or in NaCl 0.9%–DMEM– + SVF 10%, compared to  $\text{HfO}_2$ @fucoidan NPs as shown in Fig. S8 (ESI†).

To evaluate the cytotoxicity of the NPs, the cell viability assay (Resazurin) was performed on the HUVEC cell line. After 24 h of NP incubation, as shown in Fig. 4, no toxicity was observed for HUVECs from 2 to 32 mM for both NPs, as compared to

**Table 1** Results of the multi-Gaussian models of fluorescence emission spectra. The percentage of each contribution is estimated by the area at each wavelength over the total area

%	Band I (305 nm)	Band II (381 nm)	Band III (521 nm)	Band IV (675 nm)
$\text{HfO}_2$	25	25	41	9
$\text{HfO}_2$ @citrate	24	24	43	9
$\text{HfO}_2$ @fucoidan	24	31	38	7

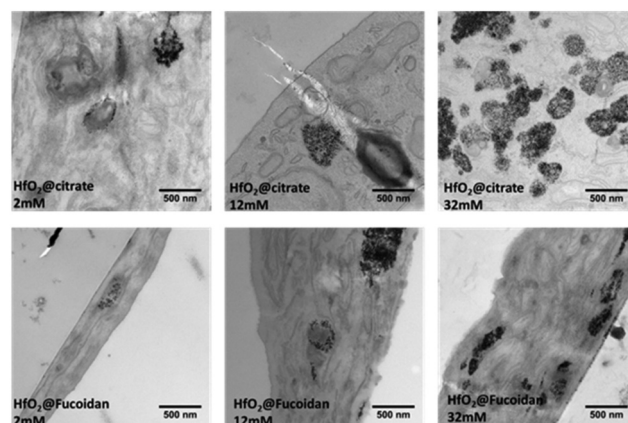


**Fig. 3** TEM images of the HUVEC cell line incubated with  $\text{HfO}_2$ @citrate and  $\text{HfO}_2$ @fucoidan at different extracellular concentrations (2 mM, 12 mM, 32 mM) for 24 h.



untreated cells. From 0 mM to 6 mM, there is no significant difference in cell viability with untreated cells. For  $\text{HfO}_2$ @citrate, an increase of cell viability is observed at 8 mM, 12 mM and 24 mM with a significant and maximum enhancement observed at 12 mM (factor 1.8). For  $\text{HfO}_2$ @fucoidan a maximum enhancement of the cell viability is observed at 12 mM and 32 mM (factor 2.6). For higher concentrations, this phenomenon disappears, and 50% cell inhibition was observed after incubation with 42 mM citrate NPs, whereas for fucoidan-NPs the cell viability remains 100%. This increase of cell viability with both NPs can be related to the interaction with cell membrane receptors and/or growth factors, thereby activating mitogenic signals or repressing growth-inhibitory signals. Beyond 8 mM and up to 32 mM, this effect seems to be stopped with citrate NPs and not with fucoidan NPs. In the latter case, it has been shown that fucoidan alone stimulated fetal bovine serum-induced HUVEC proliferation.<sup>71</sup> The mechanism of vascular cell growth modulation is still unknown, but it was postulated that fucoidan potentiates the fibroblast growth factor-1 FGF-1 mitogenic activity by stabilizing the growth factor and inhibiting FGF-2 mitogenic activity. Both effects occurred in a concentration-dependent manner. Hence, considering that the cell internalization of  $\text{HfO}_2$ @citrate NPs seems to be higher compared to  $\text{HfO}_2$ @fucoidan NPs (as observed in Fig. 3), the toxicity of  $\text{HfO}_2$ @fucoidan NPs will appear at higher extracellular concentrations and is counterbalanced by the fucoidan stimulation effect.

### Binding of $\text{HfO}_2$ -fucoidan NPs on P-selectin *in vitro*

To evaluate the ability of  $\text{HfO}_2$ @fucoidan NPs to target P-selectin under arterial blood flow conditions, it was necessary to label the NPs with a fluorophore to visualize and quantify in real-time the NP adhesion under fluorescence microscopy. The amine function of Rhodamine 123 (Rh123) was covalently linked to carboxylate functions at the outside NP surface using conventional carbodiimine chemistry, using the same conditions for both NPs (see the Experimental section). The dye labelling was more efficient (5-fold) for  $\text{HfO}_2$ @fucoidan NPs compared to  $\text{HfO}_2$ @citrate NPs, so arterial blood flow experiments (Fig. 5) were

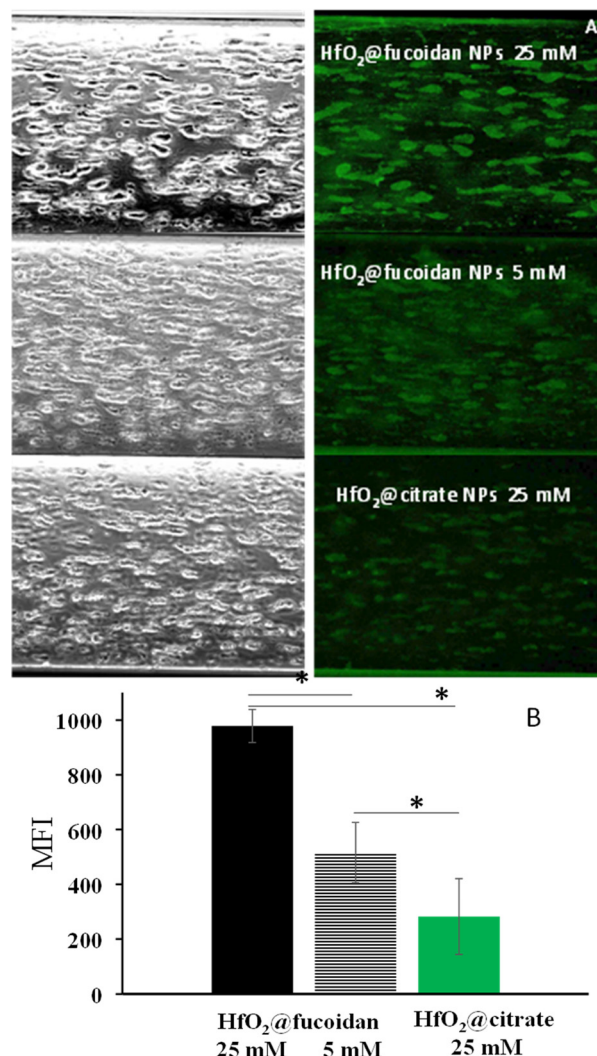


Fig. 5 Nanoparticle adhesion over platelet aggregates. Platelets adhered onto the channel wall forming aggregates expressing P-selectin (left column) and Rh123 labelled  $\text{HfO}_2$ @fucoidan NPs ([Hf] = 25 mM (top), 5 mM (middle)) and  $\text{HfO}_2$ @citrate NPs ([Hf] = 25 mM) were then injected for 5 minutes (right column). Channels were washed with 0.9% NaCl. (B) Quantitative analysis of the mean fluorescence intensity of platelet aggregates ( $n = 3$  for both NPs), \* $P < 0.05$ .

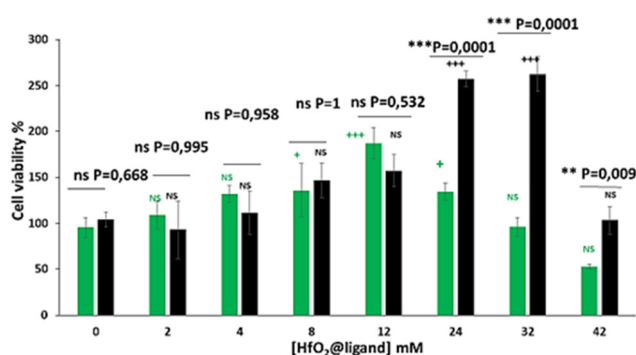


Fig. 4 HUVEC cell viability after 24 h of incubation of various extracellular concentrations of  $\text{HfO}_2$ @citrate (green bars) and  $\text{HfO}_2$ @fucoidan (black bars) NPs.

performed at the iso-nanoparticle concentration ([Hf] = 25 mM) and iso-fluorescence intensity ( $\text{HfO}_2$ @fucoidan NPs: [Hf] = 5 mM and  $\text{HfO}_2$ @citrate NPs: [Hf] = 25 mM).

When passed at the arterial flow on the platelet aggregates, Rh123 labelled  $\text{HfO}_2$ @fucoidan NPs bound to the aggregates and remained attached, whereas Rh123 labelled  $\text{HfO}_2$ @citrate NPs showed almost no binding (Fig. 5A). Quantitative analysis after 5 minutes confirmed that the mean fluorescence intensity (MFI) of fluorescent NPs was significantly higher for  $\text{HfO}_2$ @fucoidan NPs ([Hf] = 25 mM, MFI = 978 ± 61; [Hf] = 5 mM, MFI = 515 ± 109) than for  $\text{HfO}_2$ @citrate NPs ([Hf] = 25 mM, MFI = 282 ± 138) (Fig. 5B). In addition, by decreasing the average number of  $\text{HfO}_2$ @fucoidan NPs (5-fold) it is clearly observed that  $\text{HfO}_2$ @fucoidan NPs adhered significantly more onto activated platelets than control NPs.





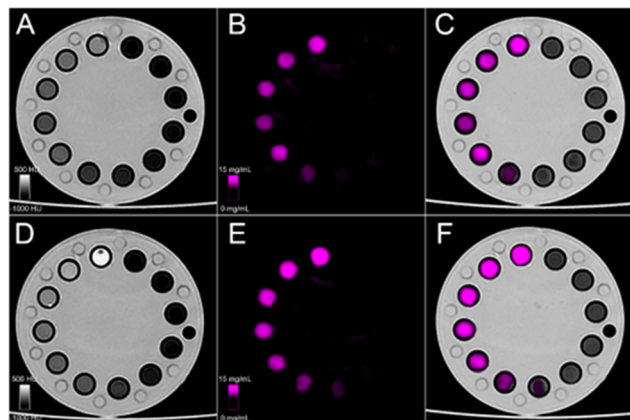


Fig. 6 Spectral photon-counting images of conventional images (A and D), K-edge images of Hafnium (purple, B and E), and fusion between K-edge and conventional images (C and F) for  $\text{HfO}_2$ @citrate NPs (top row) and  $\text{HfO}_2$ @fucoidan (bottom row).

### *In vitro* phantom imaging

Fig. 6 shows the spectral photon-counting images of conventional images (A and D), K-edge images of Hafnium (purple, B and E), and fusion between the K-edge and conventional images (C and F) for  $\text{HfO}_2$ @citrate NPs (top row) and  $\text{HfO}_2$ @fucoidan NPs (bottom row).

Conventional images provide an image of the phantom, the tubes as well as the attenuation values (Fig. 7A) while the K-edge image provides a specific and absolute quantification of the hafnium concentration found in the NPs (Fig. 7B). There was an excellent linear correlation with an  $R^2$  value very close to unity. The value of the attenuation rate (A. R.) of  $\text{HfO}_2$ @fucoidan NPs ( $27 \text{ HU ml mg}^{-1}$ ) is greater ( $\times 1.6$ ) than that of  $\text{HfO}_2$ @citrate NPs ( $17 \text{ HU ml mg}^{-1}$ ). Such a decrease of A.R. value with  $\text{HfO}_2$ @citrate NPs might be related to different mass attenuation coefficients for  $\text{HfO}_2$ @fucoidan NPs and  $\text{HfO}_2$ @citrate NPs. The photon mass attenuation coefficients are generally expressed as  $\mu/\rho$ , where  $\mu$  is the linear attenuation coefficient (in  $\text{cm}^{-1}$ ) and  $\rho$  is the material density (in  $\text{g cm}^{-3}$ ). The density of a composite made of  $\text{HfO}_2$  Nps surface functionalized with ligands (fucoidan and citrate) is  $\rho_c = \rho_{\text{ligands}} \cdot w_{\text{ligands}} + \rho_{\text{HfO}_2} \cdot w_{\text{HfO}_2}$  where  $w_{\text{ligands}}$  and  $w_{\text{HfO}_2}$  are the volume fractions of ligands and  $\text{HfO}_2$  NPs. Considering an average of

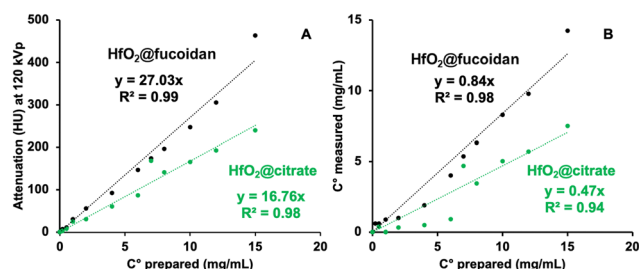


Fig. 7 Left: Attenuation rates measured for  $\text{HfO}_2$ @fucoidan (black) and  $\text{HfO}_2$ @citrate (green) with a SPCCT system. Right: Comparison between the expected and measured concentrations with K-edge imaging for  $\text{HfO}_2$ @fucoidan (black) and  $\text{HfO}_2$ @citrate (green)

65 fucoidan molecules and 800 citrate molecules per NP, a large difference in the molecular weight of the two ligands, it can be considered that the density of the composite is different considering  $\text{HfO}_2$ @fucoidan NPs and  $\text{HfO}_2$ @citrate NPs. For  $\text{HfO}_2$ @fucoidan NPs, the correlations between the measured and prepared concentrations, Fig. 7B, were strongly linear for all dilutions ( $R^2 \geq 0.98$ ). The slope (0.52) was slightly underestimated for citrate. Compared to the commercial gadolinium based molecular agent, DOTAREM<sup>®</sup> (gadoterate meglumine; Guerbet, Villepinte, France), with an attenuation rate (A. R.) equal to  $32.5 \text{ HU ml mg}^{-1}$  (Fig. S9, ESI<sup>†</sup>), the attenuation rate of  $\text{HfO}_2$ @fucoidan NPs is on the same order of magnitude (A. R. =  $27 \text{ HU ml mg}^{-1}$ ). In addition to specific targeting for the P-selectin biomarker,  $\text{HfO}_2$ @fucoidan NPs appear to be an efficient X-ray contrast agent.

## Conclusions

Atherothrombosis is the first cause of death worldwide. Early detection of atherothrombotic lesions remains a big medical challenge. In this work we have developed  $\text{HfO}_2$  NPs as computed tomography contrast agents for the detection of atherothrombosis. The nude  $\text{HfO}_2$  NPs were successfully functionalized with fucoidan or citrate and exhibited good colloidal stability in water or glucose. The fucoidan functionalized NPs allowed specific targeting of aggregated platelets under a dynamic flow test, and very good biocompatibility was demonstrated through an *in vitro* cytotoxicity assay, for high extracellular concentrations. The internalization inside the cells was confirmed with transmission electron microscopy and showed higher internalization of citrate NPs compared to fucoidan. Enhancement of the UV absorption and photoluminescence properties was observed with  $\text{HfO}_2$ -fucoidan NPs and was related to an increase of oxygen vacancies due to the reductive effect of fucoidan. The proof of concept for an efficient X-ray attenuation was illustrated through *in vitro* phantom imaging, with spectral photon counted computed tomography. The better attenuation rate observed with the fucoidan functionalized NPs compared to citrate evidenced the impact of the ligand surface on X-ray attenuation. These results confirm the ability of fucoidan coated  $\text{HfO}_2$  NPs as potential new contrast agents for X-ray imaging and particularly for the detection of atherothrombosis.

## Author contributions

Conceptualization and project administration: L. M. and P. O.; funding acquisition: P. O. and F. C.; investigation: Y. S., S. S.-M., R. A., and M. C.; data curation: Y. S. and S. S.-M., L. M.; formal analysis: Y. S., S. S.-M., F. G., and L. M.; resources: P. O., F. C., L. M., S. S.-M., and Y. L.; supervision: L. M. and P. O.; validation: Y. S., S. S.-M., R. A., and M. C.; visualization: Y. S. and L. M.; writing – original draft: Y. S. and L. M.

## Conflicts of interest

There are no conflicts to declare.



## Acknowledgements

The authors would like to acknowledge Mohammad Varasteh, PhD, CREATIS, UMR 5220, Univ Lyon, INSA Lyon, University Claude Bernard Lyon 1, Lyon, France, to perform the spectral photon-counting images of the commercial gadolinium based molecular agent: DOTAREM<sup>®</sup>, NanoMat platform of the Sorbonne Université Paris Nord for the use of UV-vis, Zetasizer Nano ZS, the ImagoSeine core facility of the Institut Jacques Monod (R. Le Borgne and C. Durieu), member of IBISA and France-BioImaging (ANR-10-INBS-04) infrastructures for TEM imaging. We warmly thank ANR to have supported our project ANR-16-CE18-0031.

## References

- 1 D. L. Steen, I. Khan, K. Andrade, A. Koumas and R. P. Giugliano, *J. Am. Heart Assoc.*, 2022, **11**, e022198.
- 2 J. Lin, Y. Chen, N. Jiang, Z. Li and S. Xu, *Front. Cardiovasc. Med.*, 2022, **9**, 868370.
- 3 K. Fujii, T. Seki, Y. Nakata, K. Atagi and T. Matsuyama, *Surg. Case Rep.*, 2022, **8**, 36.
- 4 B. Guo, Z. Li, P. Tu, H. Tang and Y. Tu, *Front. Cardiovasc. Med.*, 2021, **8**, 692915.
- 5 J. Sanz and Z. A. Fayad, *Nature*, 2008, **451**, 953–957.
- 6 K. Stark and S. Massberg, *Nat. Rev. Cardiol.*, 2021, **18**, 666–682.
- 7 G. Baidildinova, M. Nagy, K. Jurk, P. S. Wild, H. ten Cate and P. E. J. van der Meijden, *Front. Cardiovasc. Med.*, 2021, **8**, 684920.
- 8 J. W. Semple and J. Freedman, *Cell. Mol. Life Sci.*, 2010, **67**, 499–511.
- 9 K. Pluta, K. Porębska, T. Urbanowicz, A. Gsecka, A. Olasinska-Wisniewska, R. Targóński, A. Krasińska, K. J. Filipiak, M. Jemielity and Z. Krasiński, *Biology*, 2022, **11**, 224.
- 10 D. Ganesh, P. Jain, C. D. Shanthamurthy, S. Toraskar and R. Kikkeri, *Front. Chem.*, 2021, **9**, 773027.
- 11 H. Liu, G. Pietersz, K. Peter and X. Wang, *J. Nanobiotechnol.*, 2022, **20**, 75.
- 12 X. Wang, M. Ziegler, J. D. McFadyen and K. Peter, *Br. J. Pharmacol.*, 2021, **178**, 4246–4269.
- 13 C. Mayer, D. S. Cooper, A. Redfern, X. Geng, J. Shi, M. L. van Zutphen-van Geffen, I. Kuan, K. Koeck, H. Kastrissios, K. Patel, M. Davis and P. Yue, *Blood*, 2021, **138**, 977.
- 14 R. P. McEver, K. L. Moore and R. D. Cummings, *J. Biol. Chem.*, 1995, **270**, 11025–11028.
- 15 K. Wang, X. Xu, Q. Wei, Q. Yang, J. Zhao, Y. Wang, X. Li, K. Ji and S. Song, *Ther. Adv. Chronic Dis.*, 2022, **13**, 20406223221076891.
- 16 M. Kusaykin, I. Bakunina, V. Sova, S. Ermakova, T. Kuznetsova, N. Besednova, T. Zaporozhets and T. Zvyagintseva, *Biotechnol. J.*, 2008, **3**, 904–915.
- 17 B. Li, F. Lu, X. Wei and R. Zhao, *Molecules*, 2008, **13**, 1671–1695.
- 18 L. Bachelet, I. Bertholon, D. Lavigne, R. Vassy, M. Jandrot-Perrus, F. D. R. Chaubet and D. Letourneur, *Biochim. Biophys. Acta, Gen. Subj.*, 2009, **1790**, 141–146.
- 19 F. Rouzet, L. Bachelet-Violette, J. M. Alsac, M. Suzuki, A. Meulemans, L. Louedec, A. Petiet, M. Jandrot-Perrus, F. Chaubet, J. B. Michel, D. Le Guludec and D. Letourneur, *J. Nucl. Med.*, 2011, **52**, 1433–1440.
- 20 M. Suzuki, L. Bachelet-Violette, F. Rouzet, A. Beilvert, G. Autret, M. Maire, C. Menager, L. Louedec, C. Choqueux, P. Saboural, O. Haddad, C. Chauvierre, F. Chaubet, J. B. Michel, J. M. Serfaty and D. Letourneur, *Nanomedicine*, 2014, **10**, 73–87.
- 21 W. J. Bae, M. Trikeriotis, J. Sha, E. L. Schwartz, R. Rodriguez, P. Zimmerman, E. P. Giannelis and C. K. Ober, *J. Mater. Chem.*, 2010, **20**, 5186–5189.
- 22 R. Ambrosio, O. Arciniega, A. Carrillo, M. Moreno, A. Heredia and C. Martinez, *Can. J. Phys.*, 2014, **92**, 806–812.
- 23 J. Molina, A. L. Munoz, W. Calleja, P. Rosales and A. Torres, *J. Mater. Sci.*, 2011, **47**, 2248–2255.
- 24 C. Liu, T. J. Hajagos, D. Kishpaugh, Y. Jin, W. Hu, Q. Chen and Q. Pei, *Adv. Funct. Mater.*, 2015, **25**, 4607–4616.
- 25 F. N. I. Sari, S. H. Lu and J. M. Ting, *J. Am. Ceram. Soc.*, 2020, **103**, 2252–2261.
- 26 T. L. McGinnity, O. Dominguez, T. E. Curtis, P. D. Nallathamby, A. J. Hoffman and R. K. Roeder, *Nanoscale*, 2016, **8**, 13627–13637.
- 27 S. Bonvalot, C. Le Pechoux, T. De Baere, G. Kantor, X. Buy, E. Stoeckle, P. Terrier, P. Sargos, J. M. Coindre, N. Lassau, R. Ait Sarkouh, M. Dimitriu, E. Borghi, L. Levy, E. Deutsch and J. C. Soria, *Clin. Cancer Res.*, 2017, **23**, 908–917.
- 28 S. Bonvalot, P. L. Rutkowski, J. Thariat, S. Carrère, A. Ducassou, M. P. Sunyach, P. Agoston, A. Hong, A. Mervoyer, M. Rastrelli, V. Moreno, R. K. Li, B. Tiangco, A. C. Herraes, A. Gronchi, L. Mangel, T. Sy-Ortin, P. Hohenberger, T. de Baère, A. Le Cesne, S. Helfre, E. Saada-Bouazid, A. Borkowska, R. Anghel, A. Co, M. Gebhart, G. Kantor, A. Montero, H. H. Loong, R. Vergès, L. Lapeire, S. Dema, G. Kacso, L. Austen, L. Moureau-Zabotto, V. Servois, E. Wardelmann, P. Terrier, A. J. Lazar, J. Bovée, C. Le Pechoux and Z. Papai, *Lancet Oncol.*, 2019, **20**, 1148–1159.
- 29 Y. Li, Y. Qi, H. Zhang, Z. Xia, T. Xie, W. Li, D. Zhong, H. Zhu and M. Zhou, *Biomaterials*, 2019, **226**, 119538.
- 30 L. Maggiorella, G. Barouch, C. Devaux, A. Pottier, E. Deutsch, J. Bourhis, E. Borghi and L. Levy, *Future Oncol.*, 2012, **8**, 1167–1181.
- 31 R. K. Roeder, T. E. Curtis, P. D. Nallathamby, L. E. Irimata, T. L. McGinnity, L. E. Cole, T. Vargo-Gogola and K. D. Cowden Dahl, in *Society of Photo-Optical Instrumentation Engineers (SPIE) Conference Series*, 2017, vol. 10132, p. 101320X.
- 32 F. Ostadhossein, S. K. Misra, I. Tripathi, V. Kravchuk, G. Vulugundam, D. LoBato, L. E. Selmic and D. Pan, *Biomaterials*, 2018, **181**, 252–267.
- 33 F. Ostadhossein, I. Tripathi, L. Benig, D. LoBato, M. Moghiseh, C. Lowe, A. Raja, A. Butler, R. Panta, M. Anjomrouz, A. Chernoglazov and D. Pan, *Adv. Funct. Mater.*, 2020, **30**, 2070025.
- 34 C. Liu, T. J. Hajagos, D. Kishpaugh, Y. Jin, W. Hu, Q. Chen and Q. Pei, *Adv. Funct. Mater.*, 2015, **25**, 4607–4616.
- 35 D. P. Cormode, S. Si-Mohamed, D. Bar-Ness, M. Sigovan, P. C. Naha, J. Balegamire, F. Lavenne, P. Coulon, E. Roessl, M. Bartels, M. Rokni, I. Bleviss, L. Bousset and P. Douek, *Sci. Rep.*, 2017, **7**, 4784.



- 36 N. Halttunen, F. Lerouge, F. Chaput, M. Vandamme, S. Karpati, S. Si-Mohamed, M. Sigovan, L. Boussel, E. Chereul, P. Douek and S. Parola, *Sci. Rep.*, 2019, **9**, 12090.
- 37 I. Riederer, D. Bar-Ness, M. A. Kimm, S. Si-Mohamed, P. B. NoÅkl, E. J. Rummeny, P. Douek and D. Pfeiffer, *Sci. Rep.*, 2019, **9**, 5268.
- 38 S. Si-Mohamed, D. Bar-Ness, M. Sigovan, V. R. Tatard-Leitman, D. P. Cormode, P. C. Naha, P. Coulon, L. Rascle, E. Roessl, M. Rokni, A. Altman, Y. Yagil, L. Boussel and P. Douek, *Eur. Radiol. Exp.*, 2018, **2**, 34.
- 39 S. Si-Mohamed, D. P. Cormode, D. Bar-Ness, M. Sigovan, P. C. Naha, J.-B. Langlois, L. Chalabreysse, P. Coulon, I. Blevis, E. Roessl, K. Erhard, L. Boussel and P. Douek, *Nanoscale*, 2017, **9**, 18246–18257.
- 40 S. Si-Mohamed, V. r Tatard-Leitman, A. Laugere, M. Sigovan, D. Pfeiffer, E. J. Rummeny, P. Coulon, Y. Yagil, P. Douek, L. Boussel and P. B. Noel, *Sci. Rep.*, 2019, **9**, 8458.
- 41 S. Si-Mohamed, A. Thivolet, P. E. Bonnot, D. Bar-Ness, V. K  p  n  kian, D. P. Cormode, P. Douek and P. Rousset, *Invest. Radiol.*, 2018, **53**(10), 629–639.
- 42 S. A. Si-Mohamed, J. Miaillhes, P.-A. Rodesch, S. Boccalini, H. Lacombe, V. R. Leitman, V. Cottin, L. Boussel and P. Douek, *J. Clin. Med.*, 2021, **10**, 5757.
- 43 S. A. Si-Mohamed, M. Sigovan, J. C. Hsu, V. Tatard-Leitman, L. Chalabreysse, P. C. Naha, T. Garrivier, R. Dessouky, M. Carnaru, L. Boussel, D. P. Cormode and P. C. Douek, *Radiology*, 2021, **300**(1), 98–107.
- 44 A. S.-M. Salim, B. Sara, L. Hugo, D. Adja, V. Mohammad, R. Pierre-Antoine, D. Riham, V. Marjorie, T.-L. Val  rie, B. Thomas, C. Philippe, Y. Yoad, L. Elias, E. Klaus, R. Benjamin, B. Eric, R. Gilles, F. Gerard, B. Cyrille, B. Loic, G. Joel and C. D. Philippe, *Radiology*, 2022, **303**, 303–313.
- 45 N. R. van der Werf, P. A. Rodesch, S. Si-Mohamed, R. W. van Hamersvelt, M. J. W. Greuter, T. Leiner, L. Boussel, M. J. Willemink and P. Douek, *Eur. Radiol.*, 2022, **32**(5), 3447–3457.
- 46 N. R. van der Werf, S. Si-Mohamed, P. A. Rodesch, R. W. van Hamersvelt, M. J. W. Greuter, S. Boccalini, J. Greffier, T. Leiner, L. Boussel, M. J. Willemink and P. Douek, *Eur. Radiol.*, 2022, **32**(1), 152–162.
- 47 M. Sigovan, S. Si-Mohamed, D. Bar-Ness, J. Mitchell, J.-B. Langlois, P. Coulon, E. Roessl, I. Blevis, M. Rokni, G. Rioufol, P. Douek and L. Boussel, *Sci. Rep.*, 2019, **9**, 19850.
- 48 S. Boccalini, S. A. Si-Mohamed, H. Lacombe, A. Diaw, M. Varasteh, P. A. Rodesch, M. Villien, M. Sigovan, R. Dessouky, P. Coulon, Y. Yagil, E. Lahoud, K. Erhard, G. Rioufol, G. Finet, E. Bonnefoy-Cudraz, C. Bergerot, L. Boussel and P. C. Douek, *Invest. Radiol.*, 2022, **57**(4), 212–221.
- 49 Y. Sebti, T. Chauveau, M. Chalal, Y. Lalatonne, C. Lef  bvre and L. Motte, *Inorg. Chem.*, 2022, **61**, 6508–6518.
- 50 M. Juenet, R. Aid-Launais, B. Li, A. Berger, J. Aerts, V. Ollivier, A. Nicoletti, D. Letourneur and C. Chauvierre, *Biomaterials*, 2018, **156**, 204–216.
- 51 B. Li, M. Juenet, R. Aid-Launais, M. Maire, V. Ollivier, D. Letourneur and C. Chauvierre, *Adv. Healthcare Mater.*, 2017, **6**(4), 10.
- 52 E. Roessl and R. Proksa, *Phys. Med. Biol.*, 2007, **52**, 4679–4696.
- 53 S. Si-Mohamed, S. Boccalini, P.-A. Rodesch, R. Dessouky, E. Lahoud, T. Broussaud, M. Sigovan, D. Gamondes, P. Coulon, Y. Yagil, L. C. Boussel and P. Douek, *Diagn. Interventional Imaging*, 2021, **102**, 305–312.
- 54 F. Geinguenaud, I. s Souissi, R. m Fagard, Y. Lalatonne and L. Motte, *J. Phys. Chem. B*, 2014, **118**, 1535–1544.
- 55 H. Nguyen, E. Tinet, T. Chauveau, F. Geinguenaud, Y. Lalatonne, A. Michel, R. Aid-Launais, C. Journe, C. Lef  bvre and T. Simon-Yarza, *Molecules*, 2019, **24**, 962.
- 56 L. Deblock, E. Goossens, R. Pokratath, K. De Buysser and J. De Roo, *JACS Au*, 2022, **2**, 711–722.
- 57 N. Marinval, P. Saboural, O. Haddad, M. Maire, K. Bassand, F. Geinguenaud, N. Djaker, K. Ben Akrou, M. Lamy de la Chapelle, R. Robert, O. Oudar, E. Guyot, C. Laguillier-Morizot, A. Sutton, C. Chauvierre, F. Chaubet, N. Charnaux and H. Hlawaty, *Mar. Drugs*, 2016, **14**, 185.
- 58 B. Zhou, H. Shi, X. D. Zhang, Q. Su and Z. Y. Jiang, *J. Phys. D: Appl. Phys.*, 2014, **47**, 115502.
- 59 A. Situm, M. A. Rahman, S. Goldberg and H. A. Al-Abadleh, *Environ. Sci.: Nano*, 2016, **3**, 910–926.
- 60 S. Papernov, M. D. Brunsman, J. B. Oliver, B. N. Hoffman, A. A. Kozlov, S. G. Demos, A. Shvydky, F. H. M. Cavalcante, L. Yang, C. S. Menoni, B. Roshanzadeh, S. T. P. Boyd, L. A. Emmert and W. Rudolph, *Opt. Express*, 2018, **26**, 17608–17623.
- 61 M. Kong, B. Li, C. Guo, P. Zeng, M. Wei and W. He, *Coatings*, 2019, **9**, 307.
- 62 M. Mahdavi, F. Namvar, M. B. Ahmad and R. Mohamad, *Molecules*, 2013, **18**, 5954–5964.
- 63 Y. Liu, Q. Lan, S. Sun and Q. Yang, *RSC Adv.*, 2022, **12**, 2928–2937.
- 64 A. A. Rastorguev, V. I. Belyi, T. P. Smirnova, L. V. Yakovkina, M. V. Zamoryanskaya, V. A. Gritsenko and H. Wong, *Phys. Rev. B: Condens. Matter Mater. Phys.*, 2007, **76**, 235315.
- 65 A. Y. Maslov and O. V. Proshina, *Semiconductors*, 2005, **39**, 1076–1081.
- 66 S. A. Elizi  rio, L. S. Cavalcante, J. C. Sczancoski, P. S. Pizani, J. A. Varela, J. W. M. Espinosa and E. Longo, *Nanoscale Res. Lett.*, 2009, **4**, 1371.
- 67 B. Choudhury and A. Choudhury, *Phys. E*, 2014, **56**, 364–371.
- 68 A. R. Gheisi, C. Neygandhi, A. K. Sternig, E. Carrasco, H. Marbach, D. Thomele and O. Diwald, *Phys. Chem. Chem. Phys.*, 2014, **16**, 23922–23929.
- 69 H.-M. Xiong, *J. Mater. Chem.*, 2010, **20**, 4251–4262.
- 70 G. E. Brown, V. E. Henrich, W. H. Casey, D. L. Clark, C. Eggleston, A. Felmy, D. W. Goodman, M. Gr  tzel, G. Maciel, M. I. McCarthy, K. H. Neilson, D. A. Sverjensky, M. F. Toney and J. M. Zachara, *Chem. Rev.*, 1999, **99**, 77–174.
- 71 J.-L. Giraux, S. Matou, A. E. Bros, J. Tapon-Bretonni  re, D. Letourneur and A.-M. Fischer, *Eur. J. Cell Biol.*, 1998, **77**, 352–359.

